PCCP

Stability and Activity of Titanium Oxynitride Thin Films for the Electrocatalytic Reduction of Molecular Nitrogen to Ammonia at Different pH Values

Journal:	*Physical Chemistry Chemical Physics*
Manuscript ID	CP-ART-03-2023-001330.R1
Article Type:	Paper
Date Submitted by the Author:	19-Jun-2023
Complete List of Authors:	Chukwunenye, Precious; University of North Texas, chemistry Ganesan, Ashwin; University of North Texas, Chemistry Gharaee, Mojgan ; University of North Texas, Chemistry Balogun, Kabirat; University of North Texas, Chemistry Adesope, Qasim; University of North Texas, chemistry Amagbor, Stella; University of North Texas, chemistry Golden, Teresa; University of North Texas, chemistry D'Souza, francis; University of North Texas, chemistry Cundari, Thomas; University of North Texas, Chemistry Kelber, Jeffry; University of North Texas, Department of Chemistry

SCHOLARONE™
Manuscripts

ARTICLE

Stability and Activity of Titanium Oxynitride Thin Films for The Electrocatalytic Reduction of Nitrogen to Ammonia at Different pH Values

Precious Chukwunenye,[a] Ashwin Ganesan,[a] Mojgan Gharaee,[a] Kabirat Balogun,[a] Qasim Adesope,[a] Stella Chinelo Amagbor,[a] Teresa D. Golden,[a] Francis D'Souza,[a] Thomas R. Cundari,[a] and Jeffry A. Kelber[a]*

The production of ammonia for agricultural and energy demands has accelerated research for more environmentally-friendly synthesis options, particularly the electrocatalytic reduction of molecular nitrogen (nitrogen reduction reaction, NRR). Catalyst activity for NRR, and selectivity for NRR over the competitive hydrogen evolution reaction (HER), are critical issues for which fundamental knowledge remains scarce. Herein, we present results regarding the NRR activity and selectivity of sputter-deposited titanium nitride and titanium oxynitride films for NRR and HER. Electrochemical, fluorescence and UV absorption measurements show that titanium oxynitride exhibits NRR activity under acidic conditions (pH 1.6, 3.2) but is inactive at pH 7. Ti oxynitride is HER inactive at all these pH values. In contrast, TiN – with no oxygen content upon deposition – is both NRR and HER inactive at all the above pH values. This difference in oxynitride/nitride reactivity is observed despite the fact that both films exhibit very similar surface chemical compositions – predominantly Ti^{IV} oxide – upon exposure to ambient, as determined by *ex-situ* X-ray photoelectron spectroscopy (XPS). XPS, with *in-situ* transfer between electrochemical and UHV environments, however, demonstrates that this Ti^{IV} oxide top layer is unstable under acidic conditions, but stable at pH 7, explaining the inactivity of titanium oxynitride at this pH. The inactivity of TiN at acidic and neutral pH is explained by DFT--based calculations showing that N_2 adsorption at N-ligated Ti centers is energetically significantly less favorable than at O-ligated centers. These calculations also predict that N_2 will not bind to Ti^{IV} centers due to a lack of π-backbonding. *Ex-situ* XPS measurements and electrochemical probe measurements at pH 3.2 demonstrate that Ti oxynitride films undergo gradual dissolution under NRR conditions. The present results demonstrate that the long-term catalyst stability and maintenance of metal cations in intermediate oxidation states for pi-backbonding are critical issues worthy of further examination.

1.   Introduction

The electrocatalytic reduction of molecular nitrogen to ammonia – essential to agriculture and of increasing importance for energy applications – is being extensively explored as an energy- and environmentally-friendly alternative to the high-temperature Haber-Bosch process, which currently accounts for ~ 1 - 2% of World energy consumption.[1-3] Challenges that have plagued catalyst development, however, include low selectivity for NRR over competing reactions (especially HER), and slow reaction kinetics.[4-6] Aside from the activity of the electrocatalyst, stability, and durability are also of significant importance.[7] Earth-abundant transition metal oxides and nitrides, and less commonly oxynitrides, have been evaluated as possible electrocatalysts for the reduction of nitrogen to ammonia. Several review articles have been published on transition metal-based electrocatalysts[7-14] including single- and dual-atom catalysts[15] and their activities in different media.[7-15]

An advantage of metal oxynitrides is the tunability of the N:O composition, and thus their catalytic properties, which then alter the mechanistic pathways for NRR.[16] Vanadium and cobalt oxynitrides deposited by sputter deposition have been shown to be NRR active at various pH values,[17-19] in agreement with previous studies of VN nanoparticles that indicated oxynitride surface formation as being essential for NRR.[20,21] In contrast, O-free VN films were shown to be NRR inactive under the same conditions.[22] In a seminal paper, Kang *et al*. reported that although O-free TiN films were NRR inactive, O_2 plasma oxidation of TiN to produce a titanium oxynitride layer resulted in NRR activity, with Faradaic efficiency (FE) of 9.1% at −0.6 V (vs. RHE) in 0.1 M Na_2SO_4 solution at pH 3.2, and an ammonia yield rate of 3.32×10^{-10} mol s^{-1} cm^{-2}.[12] These researchers also reported that increasing oxygen content in titanium oxynitride films improved ammonia production, which was confirmed using isotopic measurements.[12] Likewise, our group reached a similar conclusion for O-rich vanadium oxynitrides. These studies thus establish an interesting trend of NRR inactivity for

a. Department of Chemistry, University of North Texas, 1155 Union Circle, #305070, Denton, TX 76203-5017, USA.
* Jeffry.kelber@unt.edu

the O-free nitrides of V and Ti, and NRR activity for the corresponding oxynitrides, at least over a limited range of pH.

With respect to existing studies of NRR in transition metal oxynitrides, it is generally believed, based on $^{15}N_2$ studies, that a Mars-van Krevelen (MVK) NRR mechanism is operative, in which reduction of lattice N to NH_3 is coupled with the replacement of lattice N from N_2.[5,20] Recent studies of V oxides[18] and V and Co oxynitrides,[17,19] however, indicate that an MVK mechanism does not occur under the conditions tested, and that reduction of lattice N and N_2 occurs by parallel reaction mechanisms that are energetically favored at O-ligated metal centers. The existence or non-existence of an MVK reaction mechanism is not an abstract issue. The reduction of lattice N and N_2 without N incorporation into the lattice will eventually lead to the depletion of lattice N and decrease or terminate oxynitride catalyst function. In this regard, it should be pointed out that the electrochemical stability and durability of electrocatalysts under NRR conditions is an issue little addressed in the literature.[23,24]

At issue, therefore, with respect to Ti oxynitride, are (a) how lattice O and N interactions and oxynitride surface structure impact NRR reactivity and selectivity vs. HER over a range of pH values; (b) whether NRR proceeds by MVK, non-MVK or parallel reaction mechanisms; and (c) the stability and durability of the electrocatalysts under NRR conditions. As described in the methods section, electrochemical measurements, GC-mass spectroscopy, absorption spectroscopy, DFT-based theoretical methods, and both *ex-situ* and *in-situ* photoemission have been integrated to address these fundamental issues. The results, as discussed below, indicate that in common with V oxynitrides, lattice O/Ti interactions enhance N_2 binding and reduction, consistent with the inertness of O-free TiN. However, the present research also indicates that Ti oxynitride exhibits continual formation and slow dissolution of a Ti^{IV} oxide surface layer under acidic conditions. NRR activity is inhibited at pH 7 due to the stability of Ti^{IV} oxide overlayer at this pH, and its inability of this d^0 metal ion to bind N_2. Taken together, the results presented herein, in conjunction with literature precedents, indicate that the stability of oxynitride and related catalysts under specific catalyst operating conditions is a major issue deserving further examination.

2. Methods

2.1 Sample deposition

The titanium oxynitride samples were deposited on commercially available 1cm x 1cm fluorinated tin oxide (FTO) substrates using a turbomolecularly-pumped magnetron sputter deposition system with a commercial DC magnetron source (Meivac, Inc.), as described previously (base pressure – 7 x 10^{-9} Torr).[17-19,25] Substrates for sputter deposition were annealed in oxygen at 10^{-6} Torr to 900 K for 2 hrs prior to deposition to remove contaminants. Sputter deposition was carried out at a substrate temperature of 675 K, using a plasma environment consisting of 1 x 10^{-6} O_2, and 4 mTorr Ar/N_2 (1:4), at a power of 25 W for 30 min. For the films made as pure

titanium nitride prior to exposure, no oxygen was introduced. Electronic grade gases were used without further purification. A commercially available Ti sputter target, 99.9% pure, with a diameter of 1.3 inches was used for deposition. The substrate-to-sample distance was 3 inches, and the sample thickness was estimated to be > 500 Å, based on previous experiments and calculations under similar conditions.[18,19]

2.1 Film characterization

Deposited films were characterized and atomic ratios were obtained *in-situ* using a commercial Auger single-pass cylindrical mirror analyzer with a concentric electron gun (ESA 100; STAIB Instruments). Auger spectra were recorded at 3 keV incident electron beam energy. Due to the overlap in kinetic energy of the Ti (LMM) and N (KLL) peaks, the equation below was used to calculate the N/Ti atomic ratio as reported by Melnik *et al.*[26]

$$\frac{C_N}{C_{Ti}} = \frac{\alpha Ti(1) - Ti(2)}{2Ti(2)}$$

In the above equation, Ti(1) is the intensity of the overlapping Ti (LMM) and N (KLL) peaks; Ti(2) is the second Ti peak and α = Ti(2)/Ti(1) for pure Ti was found to be 0.8 for our installation.

Subsequent to ambient exposure, samples were transferred to a second vacuum system for XPS analysis.[27] XPS spectra were obtained in constant pass energy mode (23.5 eV) using a commercial 140 mm hemispherical analyzer (Physical Electronics) with a micro-channel plate detector, and Al Kα radiation from an unmonochromatized source operated at 300 W and 15 keV. Analysis of XPS data was done by established methods.[28] Peak fitting employed Gaussian–Lorentzian components as described by Milosev *et al*.[29] XPS binding energies were calibrated to C_{1s} at 284.8 eV.[30]

Several of the deposited films were used for X-ray diffraction (XRD) and scanning electron microscopy (SEM). XRD was carried out using a Rigaku SmartLab SE Powder X-ray Diffractometer with Cu Kα radiation (λ = 1.541 Å). Scanning Electron Microscopy/energy-dispersive X-ray spectroscopy (SEM/EDX) data were obtained using a JEOL JSM-IT-200 InTouchScope instrument in high vacuum mode.

2.2 Electrochemical measurements

A three-electrode setup was used to check the electrochemical activity of the films. All the experiments were carried out using an EG&G 263A potentiostat/galvanostat, having Ag/AgCl and platinum as reference and counter electrodes, respectively. The preliminary electrocatalytic activity was tested by recording linear sweep voltammograms (LSVs) for the titanium oxynitride (TiO_xN_y) and titanium nitride (TiN) films at pH 3.2. The electrolyte used was 0.1 M Na_2SO_4, with separate measurements performed in electrolytes saturated with N_2 or Ar. [19] Control studies were also performed under the same conditions using the bare FTO. Multicyclic voltammograms were recorded in both N_2 and Ar-saturated electrolytes to check the electrochemical stability of the films. To corroborate these results, an electrochemical probe (sensing) method was

utilized, in which ferricyanide was used to monitor film stability. Cyclic voltammograms were recorded for the ferricyanide solution using the TiO_xN_y film and its response was compared to that of the bare FTO. Here, the cyclic voltammograms of ferricyanide/ferrocyanide redox couple on the poorly conductive FTO/TiO_xN_y surface are expected to result in a large peak-to-peak separation due to large IR-drop. However, on bare FTO, having a relatively better-conducting surface, such peak-to-peak separation is expected to be close to that expected for a reversible redox couple in a non-aqueous solvent system. If the cyclic voltammograms of the TiO_xN_y film did not become comparable to that of bare FTO during an extended immersion period, then the film was considered stable. The N_2 from the gas line was passed sequentially via two traps containing 0.1 M HCl and 0.1 M KOH to avoid any possible basic or acidic contaminants.

Bulk electrolysis measurements were performed at -0.95 V vs. Ag/AgCl for TiO_xN_y and TiN films for 90 minutes to quantify the amount of ammonia formed from NRR. The electrolyte was saturated with N_2 gas before the experiment. The electrolyte was 0.1 M Na_2SO_4 (pH 3.2). The electrolyte (10 mL) after the electrolysis was mixed with 0.5 mL of 0.55 M NaOH containing 5 wt% salicylic acid and sodium citrate, 100 µL of sodium nitroprusside dehydrate, and 100 µL of sodium hypochlorite to generate indophenol blue dye from the ammonia formed during the bulk electrolysis experiment.[17,31] Absorbance of the indophenol blue dye was measured at 693 nm using a JASCO V-670 spectrophotometer. The same experimental setup and procedure were followed under an argon environment as a control. Time-dependent absorbance measurements were also carried out after intermittent electrolysis to evaluate the rate of ammonia production.

Hydrazine, another possible product of NRR, was also quantified using the Watt and Chrisp method.[12] A solution of p-$C_9H_{11}NO$ (5.99 g), HCl (30 mL), and C_2H_5OH (300 mL) was first

electrolysis was mixed with 9.0 mL of 1.0 M HCl and 5.0 mL of color reagent and rapidly stirred at room temperature. After incubating for 20 min, the absorbance was measured at 455 nm.

Combined ultra-high vacuum/electrochemistry (UHV-EC) was used to study changes in surface composition due to exposure to aqueous environments at controlled potential without sample exposure to ambient. This system has been previously described.[32,33] Briefly, it consists of a UHV analytical system with XPS and an ion-sputtering gun (the same as used for *ex-situ* film characterization described above), an antechamber with the electrochemical cell, and a smaller sample introduction chamber. Sample emersion from the electrolyte occurs under controlled potential, followed by rinsing in DI water to remove dried electrolyte layers, followed by transfer under vacuum to the UHV analysis chamber.

2.3 Computational studies

Density functional theory calculations were carried out within the Vienna Ab initio Simulation Package (VASP).[34] The nuclei and core electrons were replaced by exchange-correlation (XC) functionalities and appropriate pseudopotentials. The simulations were spin-polarized and based on the generalized gradient approximation (GGA) as well as projector-augmented wave (PAW) theory.[35] A Monkhorst–Pack approach was used to sample the Brillouin zone.[36]

For accurate surface energies, the energy cutoff and K-point mesh were 500 eV and 3 x 3 x 1, respectively. Since the modeled reactions occur on catalyst surfaces, the supercell size was increased in the c direction to avoid periodic images from interfering with one another; the computations used a vacuum space of 20 Å (c lattice constant ~ 29 Å). In all model slabs, the bottom three atomic layers were fixed, and the top five atomic layers and absorbed groups were relaxed. A titanium oxynitride surface in a rock salt (rs) structure was modeled. Surface DFT
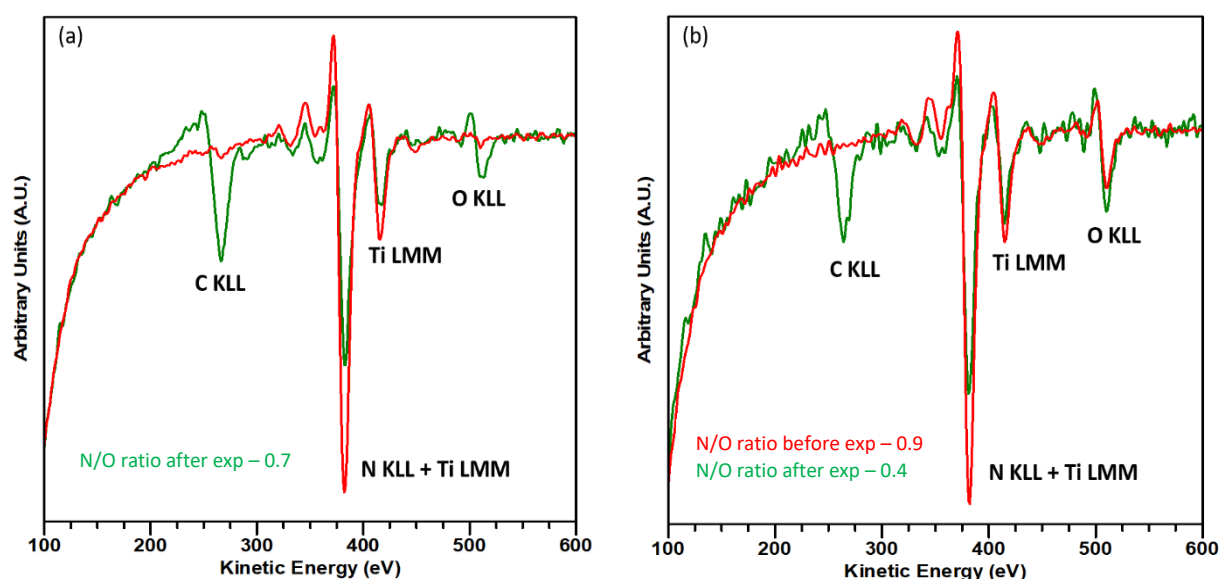

Figure 1: In-situ AES spectra after deposition and before ambient exposure (red trace) and also after 40 min ambient exposure (green trace) of (a) TiN sample; (b) TiON sample.

mixed to form a color reagent. The electrolyte (1 mL) after

calculations were done using the most stable (001) Miller-index

facet. To mimic an rs-TiO_xN_y (001) surface that was O-rich, a unit cell of 8.09 Å x 8.09 Å x 28.79 Å, with the top two layers of titanium/oxygen, followed by six layers of titanium/nitrogen was used. In total, the slab model to simulate rs-TiO_xN_y had eight layers. By using the grand-canonical approach, a Nernstian behavior can be reproduced without affecting the electrochemical control parameters and pH by the free energy of adsorbate.[37]

3. Results and Discussion

3.1 Experimental results

3.1.1 Characterization of Sputter-Deposited Films.

In-situ AES of TiN films taken after deposition showed the presence of only titanium and nitrogen for the 'pure' titanium nitride (in-situ AES N/Ti ratio ~ 1) samples, as in Fig. 1a. AES-derived elemental analysis is complicated by overlap between the Ti (LMM) and N (KLL) features (e.g., Fig. 1a), which was addressed by a procedure reported previously and described above in the methods section.[26] Upon ~40 min ambient exposure, oxidation is observed, with the presence of an oxygen peak and an AES-derived N/O atomic ratio of 0.7 (Fig. 1a). An oxidation study of a pure TiN sample was done, which revealed gradual oxidation of the sample with an increase in oxygen exposure; see Supplementary Information, Fig. S1. For the titanium oxynitride sample, in-situ AES peaks showing the presence of titanium, oxygen, and nitrogen are observed before and after ambient exposure, with slightly increased oxygen content after exposure, as shown in Fig. 1b. For the titanium oxynitride, AES-derived N/O atomic ratios before and after ambient exposure are 0.9 and 0.4 respectively. Although the

thickness of the samples was not measured directly; an estimate according to the manufacturer's manual for the Meivac sputter gun indicates film thicknesses > 500 Å.[38] The AES data in Fig. 1 thus demonstrate that, upon ambient exposure, TiN films undergo significant surface oxidation, but that the effect is less pronounced for Ti oxynitride films.

XPS spectra acquired in a different chamber after ambient exposure to both titanium nitride and oxynitride (Fig. 2) yielded core-level spectra with significant differences. A comparison of the Ti_{2p} spectra of the two films (Figs. 2a, d) shows a somewhat larger relative intensity near 459 eV binding energy for the TiN film (Fig. 2a), attributed to Ti^{IV}-O interactions.[29] This greater Ti^{IV} component intensity for the ambient exposed TiN film (Fig. 2a), relative to the Ti oxynitride film (Fig. 2d) is consistent with the AES spectra, acquired after ambient exposure, displayed in Fig. 1a, indicating a smaller degree of ambient-induced oxidation at the Ti oxynitride surface. Additionally, the N_{1s} spectrum of the oxynitride film (Fig. 2e) shows a significantly more intense component at lower binding energy, ~ 396.5 eV, than the corresponding spectrum for the TiN film (Fig. 2b). A similar trend was observed by Kang et $al.$ for plasma oxidation of a TiN film.[12] The O_{1s} spectra of the two films (Figs. 2c, f), however, are similar. Both O_{1s} features exhibit a main peak at 530 eV, characteristic of lattice O, and a shoulder near 532 eV attributed to OH species.[29] XPS-derived N/O atomic ratios of both films were ~1 after ambient exposure. The data in Fig. 2 demonstrate that TiN and TiO_xN_y films display significant differences in Ti and
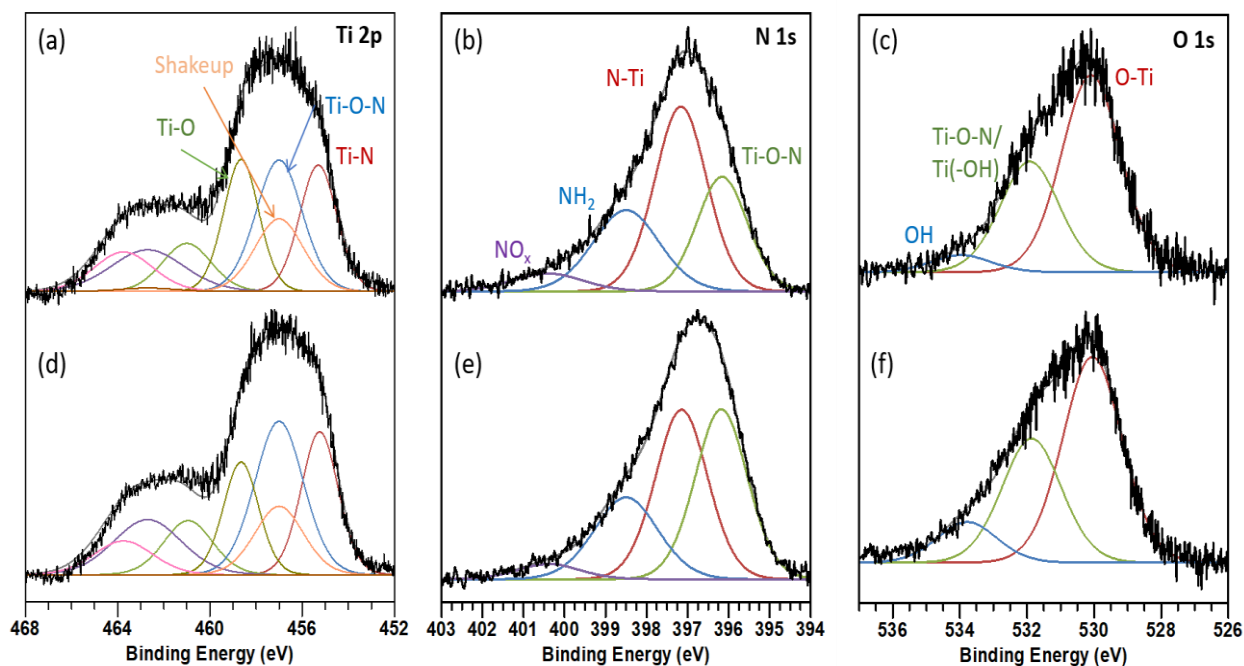
Figure 2: XPS core level spectra after ambient exposure of (a-c) 'pure' TiN sample and (d-f) a TiO_xN_y sample. The XPS-derived N/O atomic ratio is ~ 1 for both films after ambient exposure.
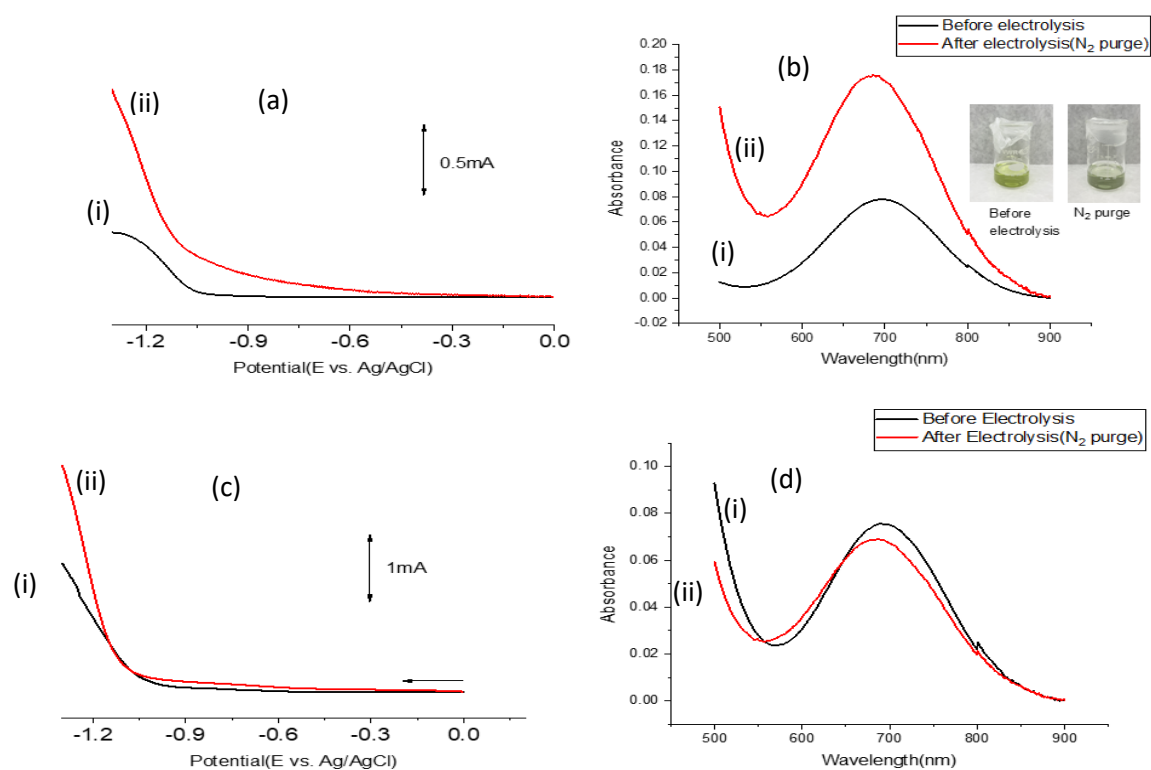
Figure 3: (a) LSV curves of (i) bare FTO (black trace) and (ii) TiO_xN_y sample (red trace); (b) absorbance before and after electrolysis in N_2 environment in 0.1 M Na_2SO_4 solution at pH 1.6; (c) LSV curves of (i) bare FTO (black trace) and (ii) TiN sample (red trace); (d) corresponding absorbance before and after electrolysis in N_2 environment in 0.1 M Na_2SO_4 solution at pH 1.6.

N core level spectra after ambient exposure, even though overall XPS-derived atomic ratios are similar.

SEM-EDX data showed no remarkable difference between the two types of films but showed spatially uniform elemental composition for both films, Fig. S2. Grazing incidence XRD data (Fig. S3) were obtained for a titanium oxynitride film with the AES-derived N/O atomic ratio of 0.4 (prior to ambient exposure) which showed the $TiO_xN_y(111)$, $TiO_xN_y(222)$ and $TiO_xN_y(220)$ features, indicative of a rock salt structure (reference according to the ICCD database JCPDS# 04-001-7608). An overlaid XRD spectrum of the bare FTO and the sample is shown in Fig S3. Using the TiON(111) and TiON(200) peaks, the average crystallite size was calculated to be 8.4 nm using the Scherrer equation. The XRD data demonstrate that the Ti oxynitride films formed by magnetron sputter deposition exhibit a bulk rock salt structure with Ti oxide overlayers induced by ambient exposure. In what follows, such films are identified as O-free titanium nitride (TiN) or titanium oxynitride (TiO_xN_y) with x and y quantified on the basis of *in-situ* AES (*i.e.*, prior to ambient exposure).

3.1.2 Electrochemical Measurements.

Linear sweep voltammograms and absorbance measurements for the detection of ammonia formation were carried on a Ti oxynitride sample, with in-situ AES-derived N:O stoichiometry of ~ 1),at pH 1.6, as shown in Figs. 3a, b. Slightly higher current was observed in N_2-saturated than in the Ar-saturated solution. The Faradaic efficiency (FE) of ammonia produced was 0.34%. An 'oxygen-free' TiN sample (per *in-situ* AES) was also tested in

similar conditions but showed no ammonia production (Figs. 3c, d).

Similar experiments were done for a TiO_xN_y film (*in-situ* AES N/O ratio ~ 1) in 0.1M Na_2SO_4 at pH 3.2, with results shown in Fig. 4. The current exhibited by the catalyst in N_2-saturated solution was higher than in Ar-saturated solution, indicating NRR activity. Ammonia formation was tested by indophenol
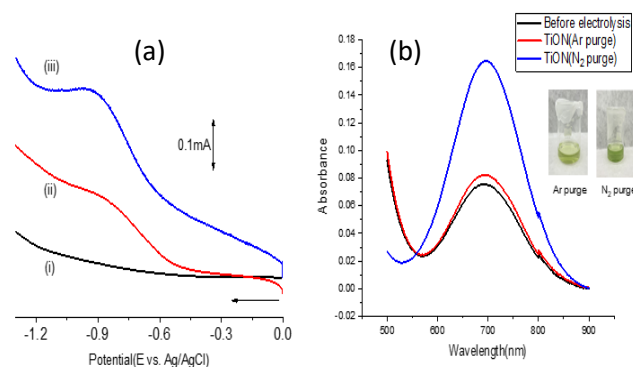
Figure 4: (a) LSV curves for (i) bare FTO (ii) TiOxNy sample in Ar-environment (iii) TiOxNy sample in N_2 environment; (b) absorbance before and after electrolysis for the detection of ammonia in Ar & N_2 – environments.
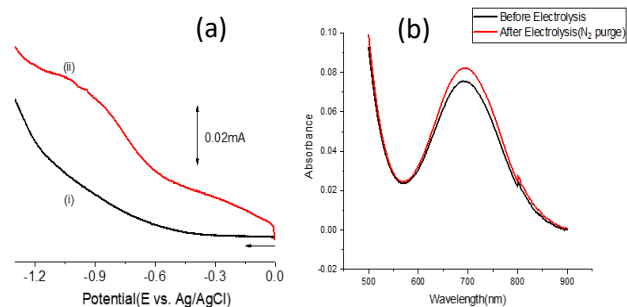
Figure 5: (a) LSV curves of (i) bare FTO and (ii) TiN sample (b)absorbance before and after electrolysis for the detection of ammonia in N2 environment in 0.1 M Na₂SO₄ solution at pH 3.2. In-situ AES N/Ti ~ 1 before ambient exposure

blue dye formation after the bulk electrolysis at -0.93 V vs. Ag/AgCl for 90 min under nitrogen and Ar-saturated systems. The bluish-green colored solution and higher absorbance at 696 nm after the addition of dye-forming agents confirm the presence of ammonia in the nitrogen-saturated solution, with a FE of 1.19%. The light greenish color in the argon environment indicates the absence of ammonia. Thus, the ammonia formed under the N_2 atmosphere is not from the lattice N. An ambient-oxidized 'pure' TiN sample was also tested for NRR activity at pH 3.2, as shown in Fig. 5. No ammonia formation was observed, indicating the importance of lattice oxygen, and not just a thin oxidized surface, for NRR activity. These results indicate substantially higher NRR activity for Ti oxynitride at pH 3.2 than at pH 1.6. To confirm that the ammonia formed is completely from N_2 and not from any NO_x contaminants, bulk electrolysis was performed using standard concentrations of sodium nitrates and nitrites.

The NRR activity of titanium oxynitride was also determined at pH 7 and 10. No significant increase in current was observed in the N_2-saturated solution for the TiO_xN_y film (*in-situ* AES N/O ratio ~1) film compared to that of bare FTO (Fig. S4). Bulk

electrolysis measurements were carried out at -0.93 V vs. Ag/AgCl at both pH values and absorbance was measured. The absence of indophenol blue dye formation from the absorbance measurements demonstrates the inactivity of the film for NRR under both pH environments. In summary, the data in Figs. 3 - 5 and S4 indicate relatively little Ti oxynitride activity at pH 1.6, significant Ti oxynitride NRR activity at pH 3.2, in agreement with previous results,[12] and no observable NRR activity at pH 7 or pH 10.

The selectivity of Ti oxynitride for NRR over the hydrogen evolution reaction (HER) was examined at pH 3.2 using GC-mass spectrometry to test for H_2 evolution. This was done by collecting gas formed during bulk electrolysis at -0.93 V vs. Ag/AgCl into the GC-thermal conductivity detector (GC-TCD) (Figs. 6a, b). The peaks at the retention times of 2.6 min and 3.8 min (Figs. 6a, b) are attributed to the formation of hydrogen and oxygen gases, respectively. A control experiment on bare FTO (Fig. 6a) gave similar results to that of a TiO_xN_y [*in-situ* AES N/O ratio ~1] film under the same conditions. A difference is the transience of O_2 evolution from the oxynitride film (Fig. 6b), suggesting at sustained oxygen evolution occurs at the FTO surface, but not at the Ti oxynitride surface, under these conditions. These experiments show the absence of significant HER for the TiO_xN_y catalyst, and (*cf.* Fig. 6a) indicates that the minimal hydrogen detected is due to the dissociation of water at -0.93V vs. Ag/AgCl. Furthermore, the TiO_xN_y film did not show any evidence of hydrazine formation at pH 3.2 when tested using the Watt and Chrisp test,[12] Fig. 6c. The HER activity of the TiO_xN_y (AES N/O ratio ~ 1) was also tested at pH 7 and 10 and showed no evolution of hydrogen at either pH in N_2-saturated solution (Fig. S5).

In summary, the above data demonstrate that Ti nitride films are NRR inactive at acidic and neutral pH. In contrast, TiO_xN_y films display NRR activity at acidic pH, but are NRR inactive at pH 7, with the ammonia produced derived from N_2
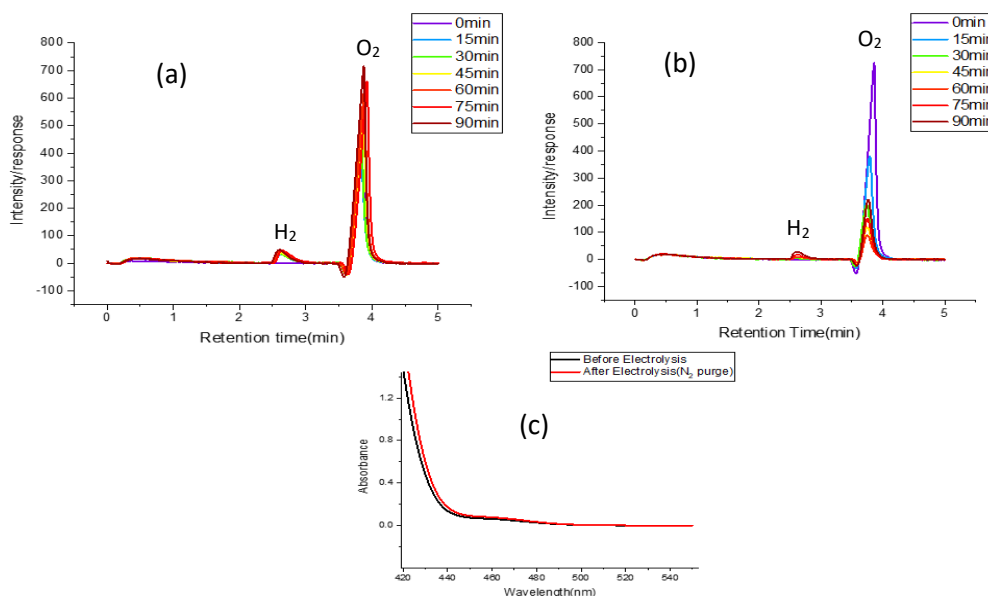
Figure 6: Gas chromatogram of (a) bare FTO and (b) TiO_xN_y during electrolysis for the detection of H_2 in N_2 environment in 0.1 M Na₂SO₄ solution at pH 3.2 (c) Absorbance before and after electrolysis for the detection of hydrazine in N_2 environment in 0.1 M Na₂SO₄ solution at pH 3.2.
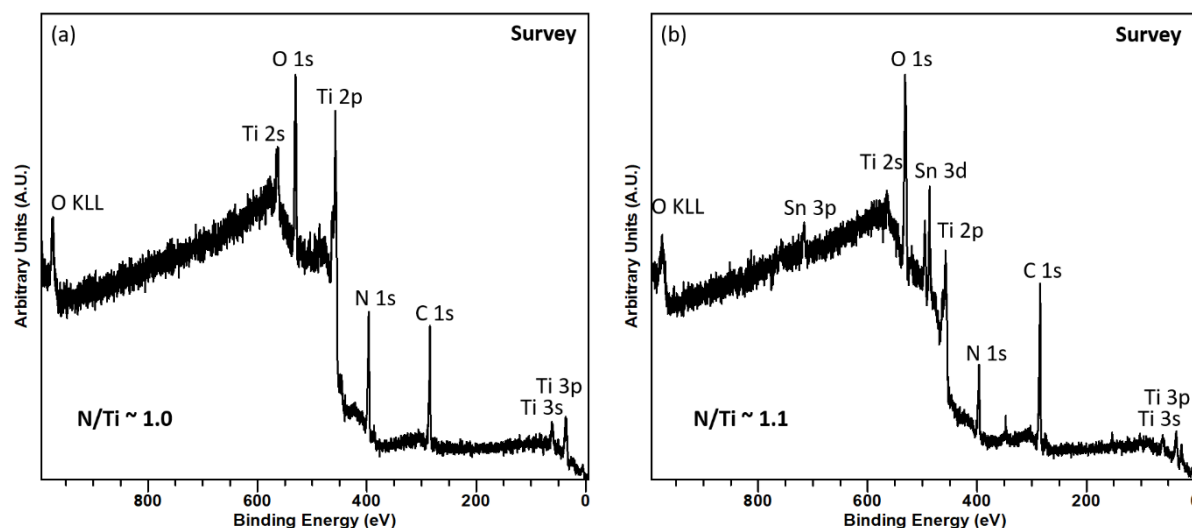
Figure 7: Ex-situ XPS survey scan of a TiON sample (a) before and (b) after 4.5 h multicyclic voltammograms at -0.93 V vs. Ag/AgCl in N_2 environment in 0.1 M Na_2SO_4 solution at pH 3.2.

rather than lattice N. Additionally, such films are HER inactive at all pH ranges tested.

A TiO_xN_y sample with *in-situ* AES N/O ratio of 1 was selected for an extended NRR experiment at the constant potential to examine catalyst durability. The *ex-situ* XPS survey spectra, Fig. 7, obtained before (Fig. 7a) and after (Fig. 7b) the electrochemical experiment, indicate a N/O atomic ratio of 1

prior to NRR (Fig. 7a) but a N/O atomic ratio of 0.4 after 4.5 hours of EC polarization at -0.93 V vs. Ag/AgCl in an N_2-saturated 0.1 M Na_2SO_4 solution at pH 3.2 (subsequent XPS spectra were acquired *ex-situ*). The presence of an Sn_{3p} peak, characteristic of the FTO substrate, after 4.5 hours of EC polarization (Fig. 7b) indicates a significant decrease in oxynitride film thickness and therefore instability of the film over long periods under these
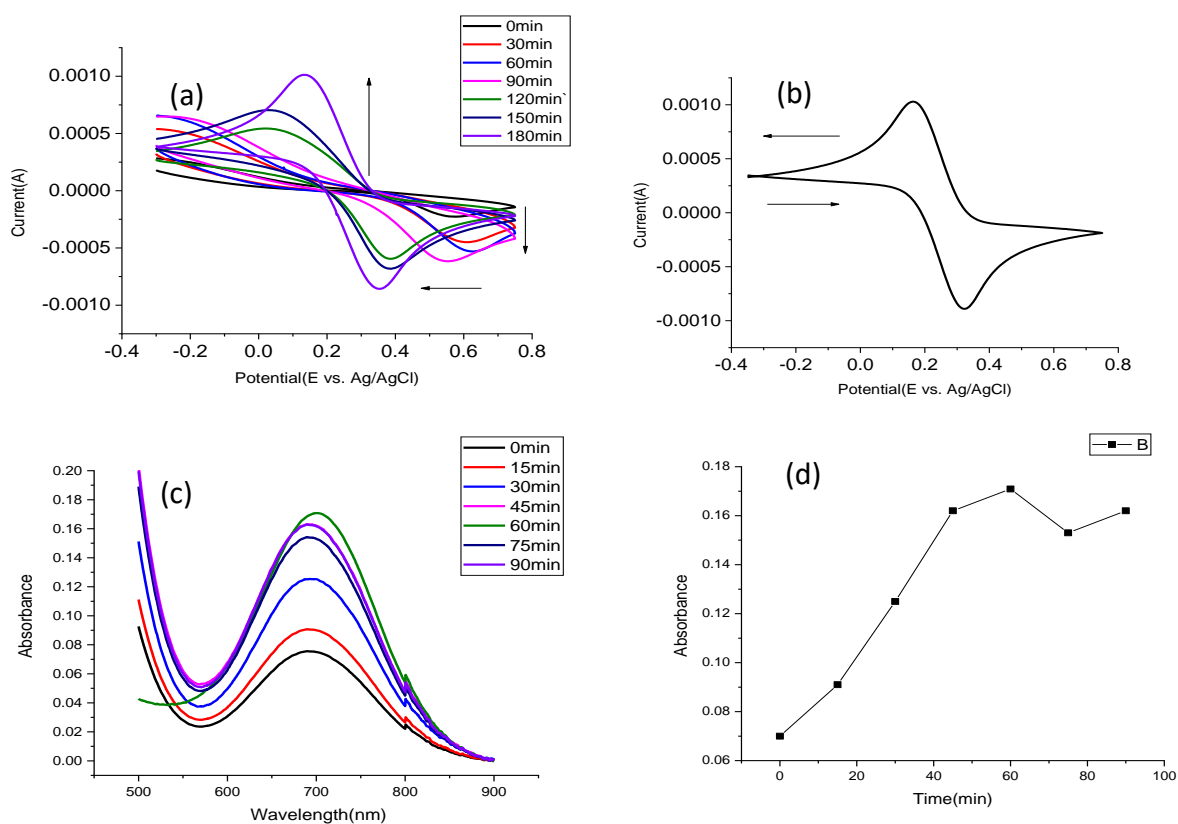
Figure 8: (a) CVs of Ferricyanide/ Ferocyanide couple with TiON film before and at intervals during electrolysis for the evaluating the stability of the film at pH 3.2, and (b) CV of Ferricyanide/ Ferocyanide couple with bare FTO. (c) Absorbance spectra before and at intervals during electrolysis at -0.93V vs Ag/AgCl for the detection of NH_3 in N_2 environment in 0.1M Na_2SO_4 solution at pH 3.2 (d) absorbance intensity/NH_3 production vs. time based on the data in (c)
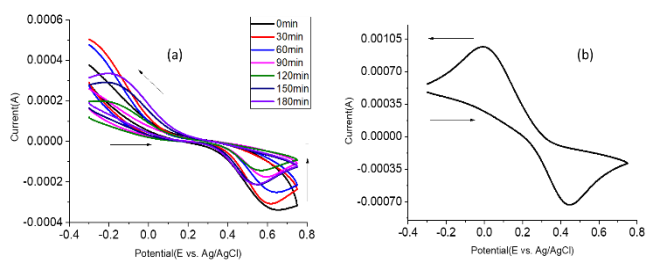
Figure 9: (a) CV's of Ferricyanide/ Ferrocyanide couple with TiON film before and at intervals during electrolysis for the evaluating the stability of the film at pH 7, and (b) CV of Ferricyanide/ Ferrocyanide couple with bare FTO in 0.1M Na_2SO_4 solution at pH 7

electrocatalysis conditions. *Ex-situ* core level XPS spectra showed an increase in the Ti-O-N/Ti-(OH) component after EC polarization, Fig. S6. Despite evident leaching of the sample after multiple cycling for over 4 hours, the N/Ti ratio remained relatively unchanged, showing the uniform loss of the electrocatalyst and not the specific loss of the lattice nitrogen. Time-dependent absorption measurements were also carried out on a fresh TiO_xN_y film during bulk electrolysis using the same potential (-0.93 V vs. Ag/AgCl) at pH 3.2, Fig. 8c. The data show a gradual increase in the rate of ammonia formation with respect to time, but a saturation point is reached after 60 min with subsequent decline. The CV and absorbance measurements (Fig. 8) are thus consistent with the XPS spectra (Fig. 7) in pointing to a gradual dissolution of Ti oxynitride films during NRR at pH 3.2.

Since titanium oxynitride films showed better Faradaic efficiency at pH 3.2 than at pH 1.6, stability experiments were carried out at pH 3.2 using the electrochemical probe(sensing) method –measuring CVs of a ferri/ferrocyanide couple – as shown in Fig. 8 to test film stability and confirm XPS results regarding the loss of material. A decrease in cathodic-to-anodic peak-to-peak separation is observed for the titanium oxynitride film (N/O ratio ~ 1), after bulk electrolysis in 30 min intervals

(Fig. 8a). The response approaches that of a bare FTO film (Fig. 8b), showing the gradual erosion of the titanium oxynitride film). This method was also utilized at pH 7 to establish the stability of a similar titanium oxynitride film (Fig. 9). No significant shift in peak-to-peak separation was observed for the film at a neutral pH after its bulk electrolysis in 30 min intervals; the response never approached that of bare FTO. These data thus indicate that the TiO_2 top layer of the TiO_xN_y film is stable at neutral pH, thus leading to the inactivity of the film at neutral pH.

UHV-EC measurements were done to determine the changes to the surface of a TiO_xN_y film surface after immersion in 0.1 M Na_2SO_4 at pH 3.2 (Fig. 10) and also at 0.1 M Na_2SO_4 at pH 7 (Fig. 11). The UHV-EC measurements at both pH values showed an increase in the Ti^{IV} component after cathodic polarization to -0.8 V and subsequent rinsing (compare Figs. 10 and 11). It should be noted that immersion times were less than a minute, but still long enough to permit the formation of a TiO_2 overlayer as evidenced by the XPS. Evidently, this overlayer is dissolved in acidic pH (Figs. 7, 8), thus allowing for continued NRR activity under acidic conditions while film dissolution occurs. The data in Fig. 11 also indicate the formation of a similar TiO_2 overlayer at pH 7, where ferricyanide/ferrocyanide CV measurements (Fig. 9) indicate overall film stability. The electrochemistry data, together with the XPS data in Fig. 11, indicate that a stable TiO_2 overlayer at pH 7 leads to NRR inactivity.

In summary, the experimental data show that the titanium oxynitride electrocatalyst is NRR active at pH 1.6, more so at pH 3.2, but inactive at pH 7 and pH 10. UHV-EC data (Figs. 10, 11) show that at both pH 3.2 and pH 7, the TiO_2 overlayer is quickly formed but XPS data (Fig. 7) and CV data (Fig. 8) show that this layer continuously dissolves at pH 3.2, which indicates that the continual evolution and dissolution of the film occurs at pH 3.2.
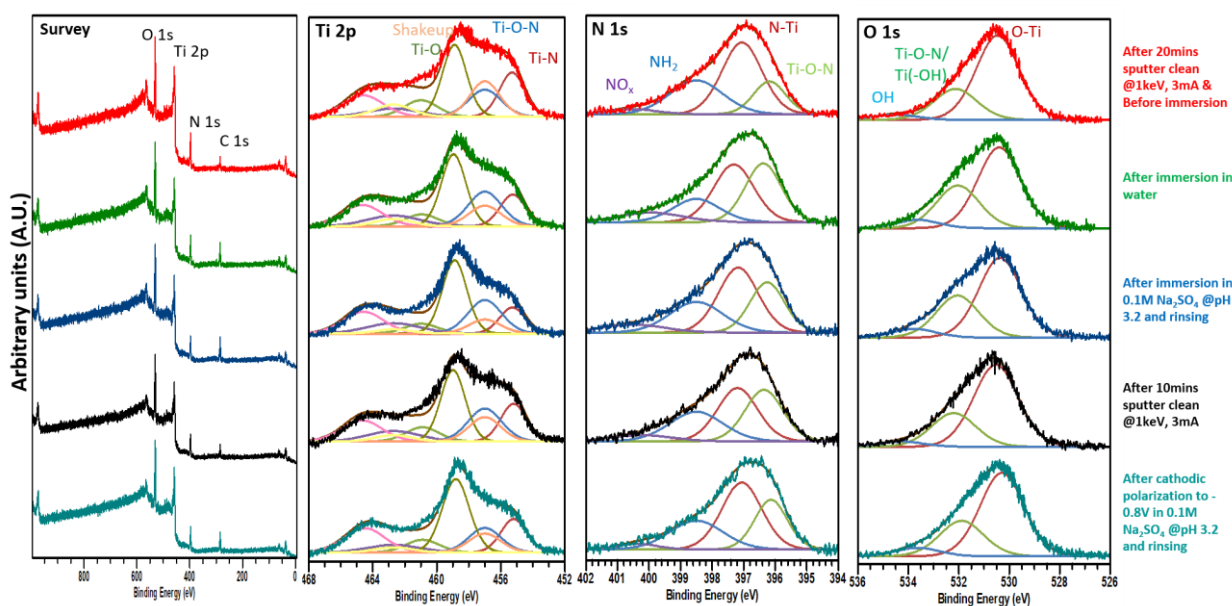

Figure 10: XPS survey scan and core level spectra of a TiON (in-situ AES Ti/O/N ratio ~1) sample for UHV-EC experiments at pH 3.2 in 0.1M Na_2SO_4 solution
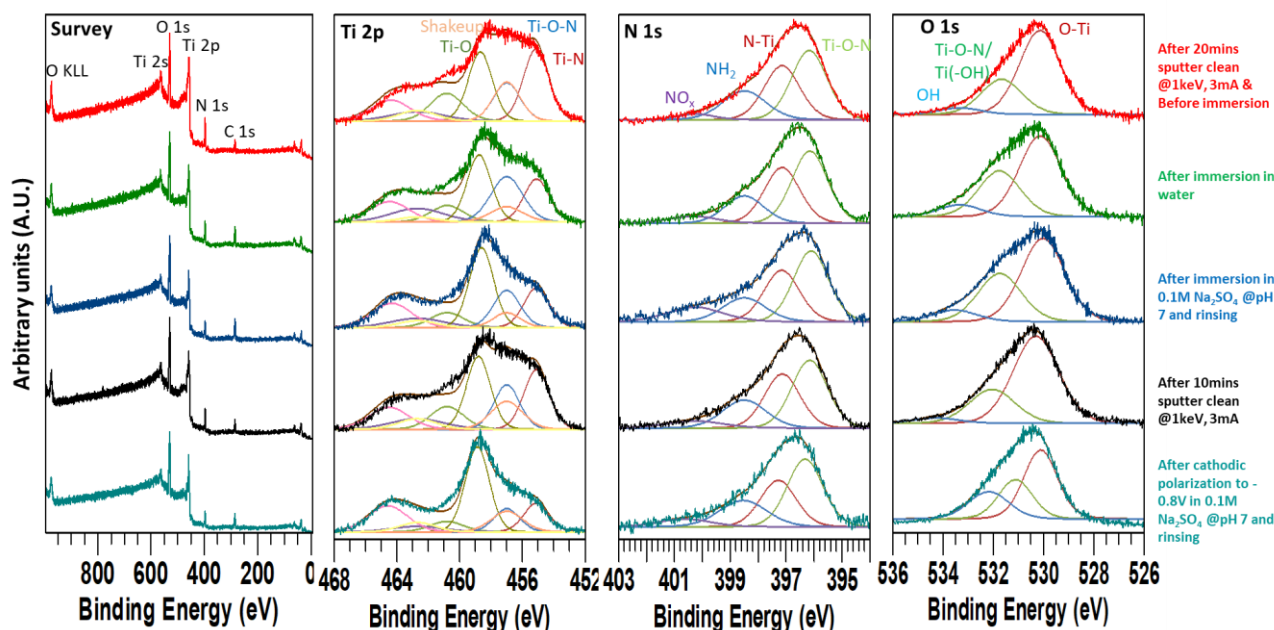
Figure 11: XPS survey scan and core level spectra of a TiO$_x$N$_y$ (in-situ AES N/O ratio ~1) sample for UHV-EC experiments at pH 7 in 0.1 M Na$_2$SO$_4$ solution.

However, the absence of dissolution of the TiO$_2$ overlayer at pH 7 is the reason for NRR inactivity at neutral pH.

3.2 Computational results

3.2.1 Modeling of *N$_a$H$_b$ surface intermediates.

Several mechanisms have been proposed for NRR, which include as a first step dinitrogen adsorption onto a surface, then activation of the strong triple bond via electron injection from an external current, and finally proton transfer from solution leading to the formation of a diazenide surface complex (*NNH).[39,40] These steps are followed by subsequent proton-coupled electron transfer (PCET) processes leading to the formation of ammonia (NH$_3$). The PCET steps are generally hypothesized to happen either via a distal or an alternating mechanism. For the former, hydrogen is first added to the outer nitrogen of *N$_2$ to form the first equivalent of ammonia, then the inner nitrogen (nearer the surface of the catalyst) is hydrogenated to produce a second equivalent of ammonia. In the alternating pathway, the first hydrogen is transferred to the outside nitrogen of *N$_2$, then a second hydrogen is attached to the inner nitrogen to form a surface-bound diazene (*NHNH), followed by alternating additional hydrogenation steps between the two nitrogen atoms of the substrate to eventually produce two equivalents of ammonia.

[TiON]-N$_a$H$_b$ (a = 1 or 2, b = 1, 2 or 3) surface configurations were modeled using plane-wave DFT calculations. A comparison of distal and alternating pathways for these configurations with pH and applied potential corrections (pH = 3.2, U = -0.5 V), eq. 1, is shown in Fig. 12.[39]

$$A\gamma_H(T, U, pH, N_H) = N_H/A_s(AG^{ads}_H (T, U, pH) + eU_{SHE} + k_B^T \ln(10) pH) \qquad (1)$$

Calculated free energies for the distal and alternating NRR pathways are shown in Fig. 12. In the presence of an applied potential of -0.5 V and assuming a pH of 3.2; the same trends in

relative energies are followed as for 0 pH and no applied potential (data not shown). Upon comparing the energy of *N$_a$H$_b$ isomers with the same number of hydrogens transferred for both distal and alternating pathways, the first hydrogen is predicted to bond to the outside nitrogen of surface-adsorbed dinitrogen to form a surface-bound diazenide, *NNH. After that, the second hydrogen was transferred to the outer nitrogen of *NNH to form *NNH$_2$ with E$_{rel.}$ to the surface of -1.44 eV for the distal pathway, Fig. 12. The third hydrogen is predicted to continue the distal pathway, eventually leading to the formation of two equivalents of ammonia.

As shown in Fig. 13, dinitrogen bonds to the model rock salt-TiO$_x$N$_y$ (001) surface, and greatly increases r$_{NN}$ from 1.09 (free dinitrogen) to 1.17 Å (*N$_2$), while the Ti-N bond length is 1.95 Å. Moreover, for intermediates in the distal pathway (the most stable pathway according to Fig. 12), the first hydrogen addition
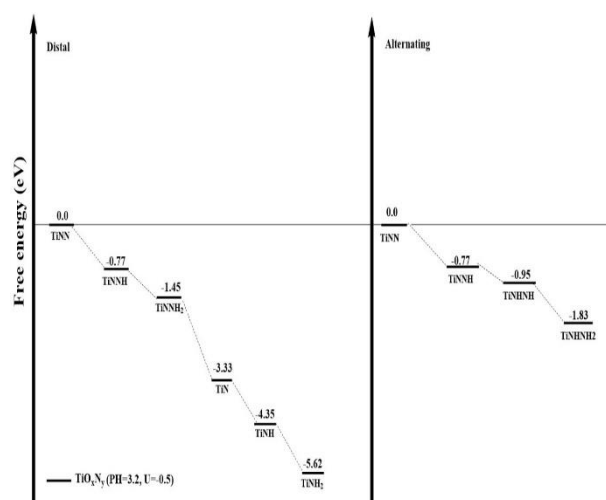

Figure 12: N/H intermediate surface configurations for distal and alternating pathways in NRR for a Ti-oxynitride model. DFT-calculated relative energies (eV), E$_{rel}$, and assume pH = 3.2 and an applied potential of -0.5 V.

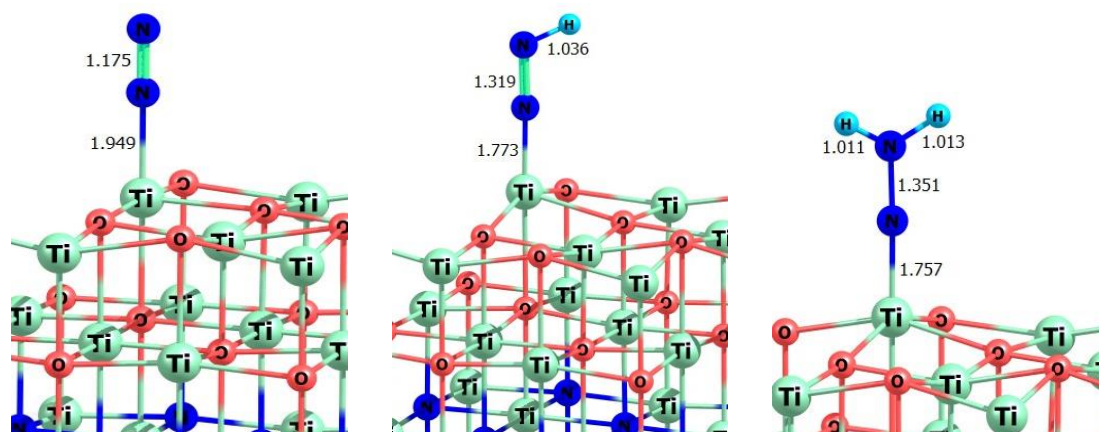**Figure 13**: DFT-optimized bond lengths for TiO_xN_y-N_2, TiO_xN_y-N_2H, and TiO_xN_y-N_2H_2 surface models; bond lengths in Å.

to the outer nitrogen of N_2 results in a significant shortening of the Ti-N bond by ~ 0.18 Å and a longer nitrogen-nitrogen bond length versus *N_2 by ~ 0.14 Å for *NNH. Bond lengths for Ti-N and N-N continue to increase, albeit by lesser amounts, by 0.02 Å for Ti-N and 0.03 Å for N-N for *NNH_2 versus *NNH. As such, there is a considerable weakening of the NN bond in the *N_2 ➔ *NNH step. According to the calculated nitrogen-nitrogen bond scission energies, *N_2 + * ➔ 2 *N is 1.64 eV, *NHNH + * ➔ 2 *NH is -2.92 eV, and *NH_2NH_2 + * ➔ 2 *NH_2 is -3.84 eV, it is plausible that nitrogen-nitrogen bond cleavage occurs after the initial reduction of the bond order to either two or one.

3.2.2 Comparison of different oxynitride models of the attached *NNH.

Using analogous plane-wave DFT results, the stability of the critical diazenide *NNH surface configuration (computations assume zero applied potential pH = 0 to facilitate comparison) was compared for the various 3d metal oxynitrides our group has studied:[17] rs-TiO_xN_y(001), rs-VO_xN_y(001), zb-CoO_xN_y(110), and zb-CoN(110), zb = zincblende.

Table 1: Calculated relative energies (in eV) of diazenide surface configuration for rs-TiO_xN_y, rs-VO_xN_y, zb-CoOxNy and zb-CoN models. Calculated from the reaction *N_2 + ½ H_2(g) = *NNH. The zincblende (zb) form has four-coordination at the metal while the rock salt (rs) morphology has six-coordination at the metal.

Model	E_{rel} (eV)
rs-TiO_xN_y-NNH	-0.09
rs-VO_xN_y-NNH	0.43
zb-CoO_xN_y-NNH	0.80
zb-CoN-NNH	1.67

The computations greatly favor the Ti oxynitride model (with a relative energy of -0.09 eV for the diazenide surface configuration). The other oxynitride models show the diazenide to be much higher in energy (Table 1) relative to *N_2. Additionally, for all of the oxynitride models we have studied thus far, the reaction coordinate goes downhill in energy after the formation of the diazenide species (Table 2) as additional H is transferred to the surface-bound substrate. An evaluation of the E_{rel} of *NNH based on calculations for the models (Table 1) thus predicts that early transition metals oxynitrides (TMONs)

like titanium and vanadium more greatly stabilize *NNH than late transition metals oxynitrides like cobalt.

Table 2: Calculated reaction energies (in eV) of *N_aH_b surface intermediates for rs-TiO_xN_y, rs-VO_xN_y, zb-CoO_xN_y and zb-CoN models. Italics denote the computed most stable tautomer.

# of H transferred	Name	E_{rel} for TiO_xN_y	E_{rel} for VO_xN_y	E_{rel} for CoO_xN_y	E_{rel} for CoN
0	*N_2	0.00	0.00	0.00	0.00
1	*NNH	-0.09	0.43	0.80	1.67
2	*NNH_2	*-0.27*	*0.02*	0.21	1.61
2	*NHNH	0.24	0.18	*-0.33*	*0.85*
3	*NNH_3	0.03	0.53	0.94	3.45
3	*N	*-1.64*	*-1.26*	-0.52	0.21
3	*$NHNH_2$	-0.14	-0.17	-3.56	*-0.92*
4	*NH	-2.16	-1.93	-1.35	-1.05
4	*NH_2NH_2	dissoc.	-1.01	*-2.63*	-0.79
5	*NH_2	*-2.93*	-2.26	-2.87	-2.79
6	*NH_3	dissoc.	*-3.34*	-2.87	-2.79

To test the role of metal on the preferred mechanism for early and late transition metals, DFT calculations were performed on rs-TiO_xN_y, rs-VO_xN_y, zb-CoO_xN_y and zb-CoN models (Table 2).

A comparison of the calculated $E_{rel.}$ of plausible reaction intermediates for the surface models (Table 2, Fig. S7) predicts that early transition metals oxynitrides like titanium and vanadium prefer the distal mechanism for NRR, while the late 3d metal oxynitride cobalt is calculated to prefer the alternating mechanism. The $E_{rel.}$ for *N – a surface nitride - for titanium and vanadium oxynitride models are more negative than the cobalt nitride and oxynitride models, Fig. S7 (Supplemental Information), reflecting the greater stability of metal-nitrogen multiple bonding for earlier transition metals. Following the production of the first equivalent of first ammonia, E_{rel} of plausible reaction intermediates declines significantly in energy to make a second equivalent of ammonia for all models, Table

2. Interestingly, *NH$_2$NH$_2$ (hydrazine) and *NH$_3$ (ammonia) is computed to be not bonded to the surface for the rs-TiO$_x$N$_y$ model (Fig. 15), but these neutral Lewis bases are ligated to a surface metal ion for the other transition metal oxynitride models.

3.2.3 Selectivity evaluation of NRR versus HER.

In general, good catalysts for NRR have high ammonia Faradaic efficiency and suppress HER activity, as well as possess the high activity and catalyst durability. In previous experimental/computational studies of V-oxides and - oxynitrides it was concluded that N$_2$/water binding was competitive under catalytic conditions.[17-19] In support of this hypothesis, N$_2$ and water binding energies for model surfaces of varying coordination number and formal oxidation state were evaluated.[17-19] N$_2$ binding was found to be favored for lower coordination numbers and less positive metal formal oxidation states, bonding characteristics that enhance π-backbonding from the metal to the N$_2$ π* orbitals. Interestingly, while the binding of water to rs-TiO$_x$N$_y$ (001) and rs-VO$_x$N$_y$ (001) surfaces is commensurate (-0.33 vs. -0.28 eV, respectively), π-backbonding in the titanium material is much stronger (-1.09 vs.

metal ions in intermediate (non-d^0) oxidation states is critical for NRR activity <u>and</u> selectivity.

4. Conclusions

The results presented herein show that pure titanium nitride and oxynitride films show little difference in surface characterization after ambient exposure, though changes can be observed in the components for the Ti and N core level XPS spectra. XRD data confirm the formation of a rock salt configuration for the Ti oxynitride films. Pure TiN films do not show NRR or HER activity at all the pH tested – 1.6, 3.2, 7, and 10. However, titanium oxynitride, shows NRR activity in acidic media, more so at pH 3.2 than 1.6. No NRR activity was recorded at neutral or basic media. Also, no HER activity was detected for titanium oxynitride at all the pH tested. This brings us to the conclusion that, on both the pure titanium nitride and titanium oxynitride samples, there is the formation of a thin titanium oxide overlayer upon ambient exposure which is unstable and dissolves in acidic media, consistent with its Pourbaix diagram. This accounts for the inactivity of pure TiN in acidic media while the oxynitride is active. However, this Ti^{IV}-oxide is stable at
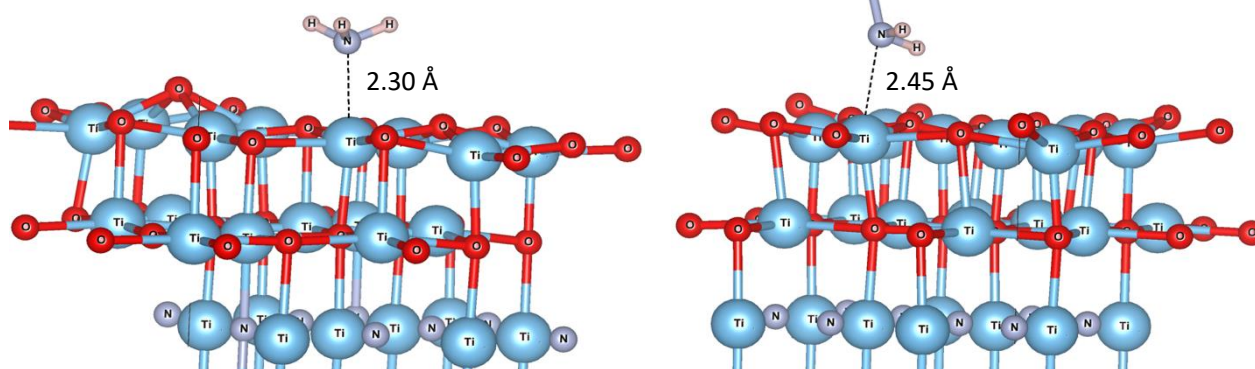

Figure 15: Geometry optimization for rs-TiO$_x$N$_y$ (001) does not result in hydrazine or ammonia being bonded to the surface.

-0.14 eV). It is posited that in the titanium oxynitrides dinitrogen is able to effectively outcompete water for binding to surface catalytic sites, thus inhibiting HER in relation to NRR. As such, maintenance of surface catalytic metal sites in intermediate oxidation states is likely critical to not only activity but selectivity of these and related NRR electrocatalysts as higher oxidation state metal ions (more Lewis acidic) are expected to favor the binding of water (Lewis base) versus N$_2$ (poor Lewis base, moderate π-acceptor),

Finally, plane-wave DFT calculations indicate that N$_2$ does <u>not</u> bind to the surface of a Ti^{IV}-oxide. For these simulations, the (110) and (111) surfaces of rutile-TiO$_2$ were tested. The lack of bonding is consistent with experiments that show that a TiO$_2$ overlayer retards NRR activity in these oxynitride materials. The inability to bind dinitrogen by d^0-Ti^{IV} ions is also consistent with the proposal that metal-to-N$_2$ π-backbonding is essential for both the binding of N$_2$ to the metal oxynitride surface and its subsequent activation. As such, the maintenance of surface

neutral pH, and pH 10, and therefore inhibits NRR activity for the titanium nitride at these pH values. DFT calculations indicate that d^0-Ti^{IV} oxides do not bind N$_2$, consistent with the observed lack of NRR reactivity at neutral and basic conditions. The present work on titanium oxynitrides – coupled with previous research on vanadium and cobalt oxynitrides[17-19] – points to the need to maintain surface metal ions in intermediate (non-d^0) formal oxidation states. Such surface states afford the potential for π-backbonding from the metal d band to N$_2$ π* orbitals, which modulates the basicity of the dinitrogen substrate and impacts the critical stability of the critical diazenide surface configuration, and may also enhance selectivity vis-à-vis HER given the differing metal-binding characteristics that N$_2$ (σ-donor and π-acceptor) and H$_2$O (σ-donor) possess.

Conflicts of interest

There are no conflicts to declare.

Acknowledgments

References

1   J. Erisman; M. Sutton, J. Galloway, Z. Klimont, and W. Winiwarter, *Nat. Geosci.,* 2008*,* **1**, 636-639.
2   L. Wang, M. Xia, H. Wang, K. Huang, C. Qian, C. Maravelias and G. Ozin, *Joule,* 2018*,* **2**, 1055-1074.
3   Y. Wan, J. Xu, and R Lv, *Mater. Today (Kidlington, England),* 2019*,* **27**, 69-90.
4   G. Qing, R. Ghazfar, S. Jackowski, F. Habibzadeh, M. Ashtiani, C. Chen, M. Smith and T. Hamann, *Chem*. *Rev.* 2020*,* **120**, 5437-5516.
5   Z. Qiao, D. Johnson, and A. Djire, *Cell Rep. Phys. Sci.* 2021*,* **2**, 100438.
6   L. Niu, L. An, X. Wang, and Z. Sun, *J. of Energy Chem.,* 2021*,* **61**, 304-318.
7   A. Liu, Y. Yang, X. Ren, Q. Zhao, M. Gao, W. Guan, F. Meng, L. Gao, Q. Yang, X. Liang and T. Ma, *Chem. Sus. Chem* 2020*,* **13**, 3766-3788.
8   Q. Liu, T. Xu, Y. Luo, Q. Kong, T. Li, S. Lu, A. Alshehri, K. Alzahrani and X. Sun, *Curr. Opin Electrochem.* 2021*,* **29**, 100766.
9   J. Pan, H. Hansen and T. Vegge, *J. Mater. Chem.,* 2020*,* **8**, 2498-2417.
10 F. Hanifpour, C. Canales, E. Fridriksson, A. Sveinbjörnsson, T. Tryggvason, E. Lewin, F. Magnus, A. Ingason, E. Skúlason and H. Flosadóttir, *Electrochim. Acta,* 2022*,* **403**, 139551.
11 B. Chang, L. Deng, S. Wang, D. Shi, Z. Ai, H. Jiang, Y. Shao, L. Zhang, J. Shen, Y. Wu and X. Hao, *J Mater. Chem.,* 2019*,* **8**, 91-96.
12 S. Kang, J. Wang, S. Zhang, C. Zhao, G. Wang, W. Cai and H. Zhang, *Electrochem Commun.,* 2019*,* **100**, 90-95.
13 Y. Yao, Q. Feng, S. Zhu, J. Li, Y. Yao, Y. Wang, Q. Wang, M. Gu, H. Wang, H. Li, X. Yuan and M. Shao, *Small Methods* 2019*,* **3**, 1800324.
14 a) L. Yang, T. Wu, R. Zhang, Z. Huang, X. Li, X. Shi, H. Zheng, Y. Zhang and X. Sun, *Nanoscale,* 2019*,* **11**, 1555-1562. b) B. Yang, W. Ding, H. Zhang and S. Zhang, *Energy Environ. Sci.,* 2021*,* **14**, 672-687.
15 a) X. Cui, C. Tang, and Q. Zhang, *Adv. Energy Mater.* 2018*,* **8**, 1800369. b) D. Wu, P. Lv, J. Wu, B. He, X. Li, K. Chu, Y. Jia, and D. Ma, *J. Mater. Chem. A* 2023*,* **11**, 1817-1828. c) D. Wu, J Wu, P. Lv, H. Li, K. Chu and D. Ma. *Small Structures*, 2023, 2200358. d) D. Ma, Z. Zeng, L. Liu, X.

16 Huang and Y. Jia, *J. Phys. Chem. C*, 2019, **123**, 19066-19076.
16 M. Sakar, R. Prakash, K. Shinde and G. Balakrishna, *Int. J. Hydrogen Energy,* 2020*,* **45**, 7691-7705.
17 P. Chukwunenye, A. Ganesan, M. Gharaee, K. Balogun, F. Anwar, Q. Adesope, T. Cundari, F. D'Souza and J. Kelber, *J. Mater. Chem.,* 2022*,* **10**, 21401-21415.
18 A. Ganesan, A. Osonkie, P. Chukwunenye, I. Rashed, T. Cundari, F. D'Souza and J. Kelber, *J. Electrochem. Soc.,* 2021*,* **168**, 26504.
19 A. Osonkie, A. Ganesan, P. Chukwunenye, F. Anwar, K. Balogun, M. Gharaee, I. Rashed, T. Cundari, F. D'Souza and J. Kelber, *ACS Appl. Mater. Interfaces,* 2022*,* **14**, 531-542.
20 X. Yang, S. Kattel, J. Nash, X. Chang, J. Lee, Y. Yan, J. Chen and B. Xu, *Angew. Chem. Int. Ed.,* 2019*,* **58**, 13768-13772.
21 X. Yang, J. Nash, J. Anibal, M. Dunwell, S. Kattel, E. Stavitski, K. Attenkofer, J. Chen, Y. Yan and B. Xu, *J. ACS,* 2018*,* **140**, 13387-13391.
22 H. Du, T. Gengenbach, R. Hodgetts and D. MacFarlane and A. Simonov, *ACS Sustainable Chem. Eng.,* 2019*,* **7**, 6839-6850.
23 Y. Abghoui and E. Skúlason, *J. Phys. Chem.,* 2017*,* **121**, 6141-6151.
24 Y. Abghoui, A. Garden, J. Howalt, T. Vegge, T and E. Skúlason, *ACS Catal.* 2016*,* **6**, 635-646.
25 A. Osonkie, V. Lee, A. Oyelade, M. Mrozek-McCourt, P. Chukwunenye, T. Golden, T. Cundari and J. Kelber, *Phys Chem. Chem. Phys.,* 2020*,* **22**, 2464-24648.
26 V. Melnik, V. Popov, D. Kruger and O. Oberemok, *Semicond. Phys. Quantum Electron.*,1999*,* **2**, 81-85.
27 B. Dong, A. Oyelade, N. Nandagopal and J. Kelber, *Surf. Coat. Technol.,* 2017*,* **314**, 45-50.
28 M. Seah and D. Briggs, 1990, pp 201-255.
29 I. Milošv, H. Strehblow, B. Navinšek, and M. Metikoš-Huković, *Surf. Interface Anal.,* 1995*,* **23**, 529-539.
30 M. Biesinger, B. Payne, A. Grosvenor, L. Lau, A. Gerson and R. Smart, *Appl Surf. Sci.,* 2011*,* **257**, 2717-2730.
31 K. Chu, Y. Liu, Y. Li, H. Zhang and Y. Tian, *J. Mater. Chem.,* 2019*,* **7**, 4389-4394.
32 M. Soriaga, *Prog. Surf. Sci.,* 1992*,* **39**, 325-443.
33 J. Kelber and G. Seshadri, *Surf. Interface Anal.,* 2001*,* **31**, 431-441.
34 J. Hafner, *J. Comput. Chem.,* 2008*,* **29**, 2044-2078.
35 G. Kresse, D. Joubert, *Phys. Rev. B, Condens. Matter,* 1999*,* **59**, 1758-1775.
36 H. Monkhorst, J. *Phys. Rev. B.,* 1976*,* **13**, 5188.
37 A. Groß, *J. Phys. Chem.,* 2022*,* **126**, 11439-11446.
38 Meivac Inc. *Owner's operation and maintenance manual of the MAK sputtering sources*, 2008.
39 T. Yang, H. Xie, N. Ma, E. Liu, C. Shi, C. He and N. Zhao, *Appl. Surf. Sci.,* 2021*,* **550**, 149355.
40 J. Hou, M. Yang and J. Zhang, *Nanoscale,* 2020*,* **12**, 69-692.